# The effect of dielectric confinement on photoluminescence of In2O3-SiO2 nanocomposite thin films incorporated by nitrogen

Yang-Ru Lyu and Tsung-Eong Hsieh

Citation: Journal of Applied Physics **113**, 184303 (2013); doi: 10.1063/1.4803877
View online: http://dx.doi.org/10.1063/1.4803877
View Table of Contents: http://scitation.aip.org/content/aip/journal/jap/113/18?ver=pdfcov
Published by the AIP Publishing

# The effect of dielectric confinement on photoluminescence of $In_2O_3$-$SiO_2$ nanocomposite thin films incorporated by nitrogen

Yang-Ru Lyu and Tsung-Eong Hsieh[a)]
*Department of Materials Science and Engineering, National Chiao Tung University, Hsinchu, 30010 Taiwan*

(Received 19 September 2012; accepted 18 April 2013; published online 9 May 2013)

Nanocomposite thin films containing $In_2O_3$ nanoparticles were prepared by the target-attachment sputtering utilizing the InN pellets and allowing the $N_2$ inlet gas flow during the deposition process. The *x*-ray photoelectron spectroscopy revealed that the chemical composition of $In_2O_3$ nanoparticles becomes $InO_xN_y$ and the $SiO_xN_y$ phase forms in the matrix of nanocomposite layer. Photoluminescence analysis indicated that the dielectric confinement effect induced by the N-incorporation tends to restrain the green emission of nanocomposite layers due to the presence of surface polarization on nanoparticles. Suppression of blue emission was also observed due to the elimination of oxygen vacancies in $In_2O_3$ nanoparticles. Furthermore, the N elements might occupy the oxygen lattice sites and generate a new defect level, $N_O^-$, to induce the violet emission. Analytical results confirmed the mechanisms of green and blue emissions of the nanocomposite thin films containing $In_2O_3$ nanoparticles reported previously. © *2013 AIP Publishing LLC*.
[http://dx.doi.org/10.1063/1.4803877]

## I. INTRODUCTION

Semiconductors of nanoscale dimensions have attracted considerable research interest owing to their unique physical properties, particularly, their luminescence properties for applications in advanced optoelectronics.[1,2] For instance, the characterizations of semiconductors in quantum dot (QD) or nanoparticle form embedded in various dielectric materials have been investigated in detail.[3–5] Indium oxide ($In_2O_3$) is a wide-bandgap semiconductor ($E_g = 3.75$ eV)[6–10] that has been subjected to extensive study on account of its versatility in applications such as solar cells,[11] gas sensors,[12] and field-emission displays.[13] The visible-light emission properties of $In_2O_3$ correlated with defect levels in the bandgap have been reported by various research groups.[6,14,15] Mazzera *et al.* observed three emission bands with peaks located at 454, 563, and 631 nm in the cathodoluminescence spectra of $In_2O_3$ samples.[6] Photoluminescence (PL) signals at 429, 460, and 637 nm were reported by Zheng *et al.*[14] and Lee *et al.*[15] during their studies on $In_2O_3$ in nanowire and thin-film forms, respectively. However, previous studies mainly investigated samples containing pristine $In_2O_3$, and the debate concerning the emission mechanism is ongoing. For instance, Orlandi *et al.*[16] and Franceschetti and Zunger[17] reported that the visible-light emissions are related to oxygen defects. Kumar *et al.* found that $In_i^{\bullet\bullet\bullet}$ is responsible for the red emission.[18] Brus[19] and Yoshimura *et al.*[20] attributed the blue-green emissions to the transitions correlated with oxygen defects. Since oxygen defect levels are unlikely to split into such a wide range in the bandgap of $In_2O_3$, further study is hence required. In addition to modulating the defect types and populations in $In_2O_3$ nanoparticles, this work also investigates the dielectric confinement effect by adding nitrogen (N) elements in the nanocomposite thin films containing $In_2O_3$ nanoparticles so as to clarify the luminescence mechanisms.

The dielectric confinement effect may occur in nanocomposite thin films containing discrete semiconductor QDs owing to the presence of surface polarizations.[16–18] Such polarizations are induced by charge accumulation on the particle surface when the dielectric mismatch presents at the QD/matrix interface. It consequently causes the confinement of electron states, and thus the dielectric confinement effect in the samples.[19–21] Because of the large specific surface area (SSA) feature of QDs, the surface states of QDs greatly affect the physical properties of nanocomposite thin films, resulting in distinctive optical and electrical properties.[22–24]

In this study, the N-incorporated nanocomposite thin films containing $In_2O_3$ nanoparticles embedded in a $SiO_2$ matrix are prepared by utilizing InN pellets and allowing $N_2$ inlet gas flow during the target-attachment sputtering process. The PL properties of samples are measured and compared with those of N-free samples in order to clarify the role of defect levels and the dielectric confinement effect on the emission properties. The microstructures and compositions of nanocomposite samples are analyzed by transmission electron microscopy (TEM) and *x*-ray photoelectron spectroscopy (XPS), respectively. Their correlations to the PL properties are discussed in order to clarify the possible origins of visible-light emissions of $In_2O_3$ proposed previously.[10]

## II. EXPERIMENT

Nanocomposite thin films containing $In_2O_3$ nanoparticles embedded in a $SiO_2$ matrix were prepared using the target-attachment method[10,25] in a sputtering system with background pressure better than $10^{-7}$ Torr. For the samples containing pristine $In_2O_3$ nanoparticles, various quantities of $In_2O_3$ pellets were mounted on a quartz target and radio-frequency (RF) magnetron sputtering deposition was then

a)Author to whom correspondence should be addressed. Electronic mail: tehsieh@mail.nctu.edu.tw

 

TABLE I. A list of sample designation, sputtering conditions, $In_2O_3$ nanoparticle diameters, and N contents of nanocomposite thin films.

| | Sputtering conditions | | | |
|---|---|---|---|---|
| Sample designation | Pellet type/Number | $N_2$/Ar ratio | Particle diameter (nm) | N content (at. %) |
| *a* | $In_2O_3$/1 | 0 | 3.1 | 0 |
| *b* | $In_2O_3$/1 | 0.05 | 3.2 | 0.5 |
| *c* | $In_2O_3$/1 | 0.15 | 3.7 | 1.4 |
| *d* | $In_2O_3$/1 | 0.25 | 3.7 | 1.8 |
| *e* | InN/1 | 0.05 | 3.6 | 0.5 |
| *f* | InN/1 | 0.15 | 3.8 | 2.3 |
| *g* | InN/1 | 0.25 | 3.6 | 2.9 |
| *h* | InN/3 | 0.05 | 3.8 | 1.0 |
| *i* | InN/3 | 0.15 | 3.5 | 3.6 |
| *j* | InN/3 | 0.25 | 3.7 | 4.5 |

carried out at a gun power of 130 W and a working pressure of 3.5 mTorr with high-purity argon (Ar) as the inlet gas flow. The nanoparticle content in the samples was adjusted by varying the number of $In_2O_3$ pellets. For the N-incorporated samples, a mixed $N_2$/Ar inlet gas flow at various ratios of 5% to 25% (in standard cubic centimeters per minute) was introduced during the sputtering. Moreover, InN pellets, instead of pure $In_2O_3$ pellets, were chosen as the source of $In_2O_3$ nanoparticles in these samples. As revealed by subsequent XPS analysis, the InN transforms into N-incorporated $In_2O_3$ with a composition in the form of $InO_xN_y$. This was ascribed to the enrichment of oxygen (O) elements in the $SiO_2$ matrix, which in turn caused the oxidation of InN. The addition of $N_2$ inlet gas flow during sputtering further increased the N content of the samples, amplifying the dielectric confinement effect on the emission properties of the nanocomposite samples. Sample designations and corresponding preparation conditions are listed in Table I.

The PL properties, microstructures, and compositions of the samples were characterized immediately after the completion of sample preparation. No post-annealing treatment was performed to modulate the structures and properties of samples. The microstructures of the nanocomposite thin films were examined by TEM (JEOL, JEM-2100F) operated at 200 kV. The evolution of the chemical bonds of the elements in the samples was analyzed by XPS (American Physical Electronics ESCA PHI 1600) using Mg-$K_\alpha$ *x*-ray excitation. The PL spectra of the samples were measured at room temperature using a self-assembly PL apparatus equipped with a 325-nm He-Cd laser.

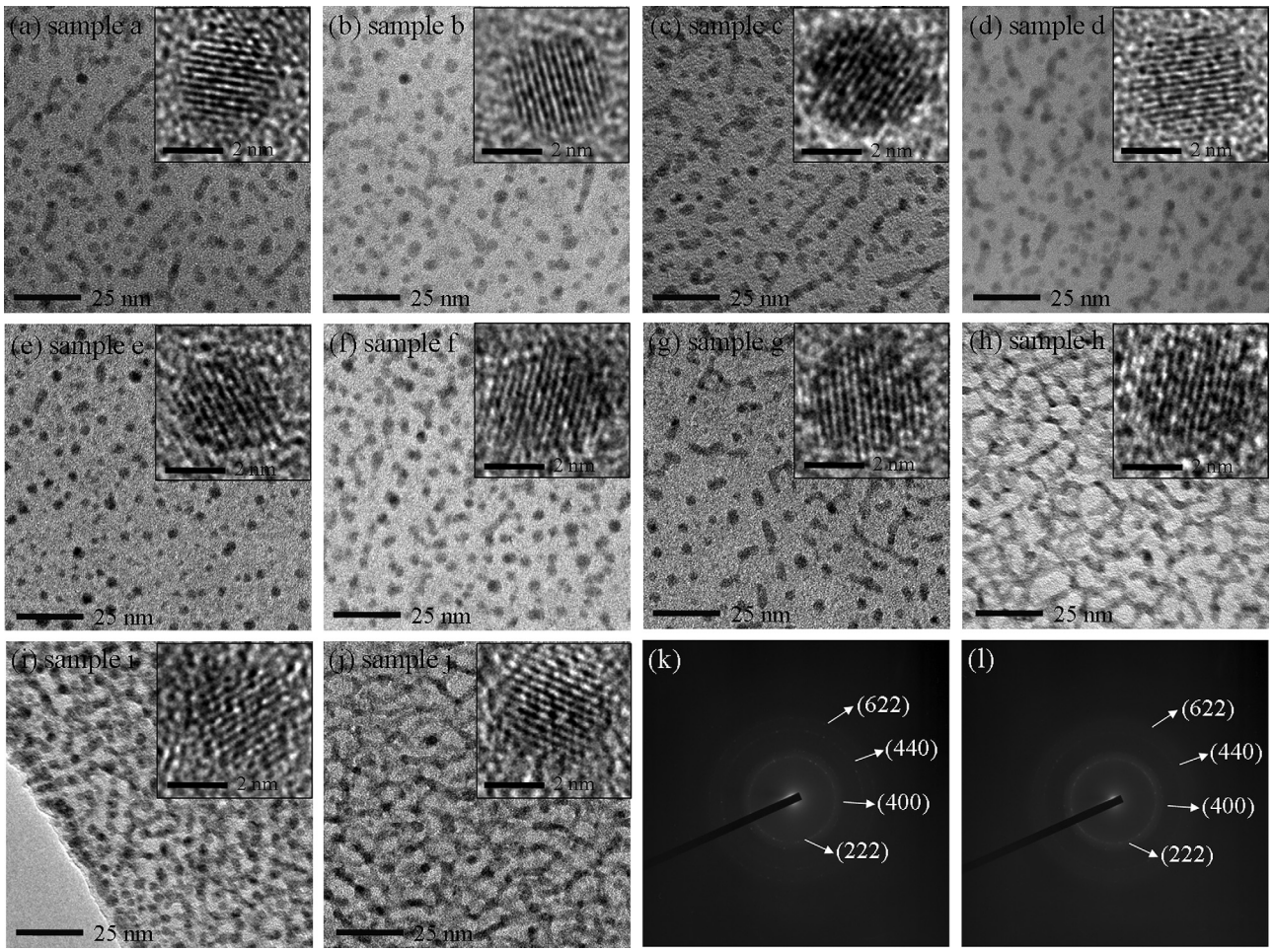


FIG. 1. TEM images (a) to (j) show the microstructures corresponding to samples *a-j*. Inset at the upper right-hand corner of each micrograph is the high-magnification images of nanoparticles. Typical SAED patterns of nanocomposite thin films prepared by using $In_2O_3$ and InN pellets are separately given in (k) and (l). The indices of SAED patterns according to JCPDS standard No.06-0416 indicated the phase type of nanoparticles is $In_2O_3$ regardless of the pellet type employed during sputtering deposition.

## III. RESULTS AND DISCUSSIONS

### A. Microstructures

Figures 1(a)–1(j) separately present the TEM micrographs of nanocomposite samples *a-j*. Inset at the upper right-hand corner of each micrograph is an enlarged image of the nanoparticles embedded in each of the samples; a single set of lattice fringes presenting the nanoparticle reveals the single crystalline form of the nanoparticles. Typical selected area electron diffraction (SAED) patterns for the samples prepared using $In_2O_3$ and InN pellets are shown in Figs. 1(k) and 1(l), respectively. The indices of the SAED patterns indicate that the phase type of the nanoparticles is body-centered cubic (BCC) $In_2O_3$, regardless of the pellet type used for sample preparation. The hexagonal InN phase was not detected in all samples; however, subsequent XPS analysis revealed the presence of N elements in the $In_2O_3$ nanoparticles. The absence of the InN phase indicates that InN transforms to N-incorporated $In_2O_3$, the result of an oxidation reaction because it was embedded in the $SiO_2$ matrix with many O elements.

InN tends to decompose at high temperatures, reportedly at temperatures higher than 550 °C.[26] The decomposition temperature of InN might be reduced in an environment with a low $N_2$ gas partial pressure and in our samples, the residual In elements might react with the surrounding to form $In_2O_3$ as follows:[27,28]

$$\mathrm{InN}_{(s)} = \mathrm{In}_{(s)} + \frac{1}{2}\mathrm{N}_{2(g)},$$

$$4\mathrm{In}_{(s)} + 3\mathrm{O}_{2(g)} = 2\mathrm{In}_2\mathrm{O}_{3(s)}.$$

The instability of InN can also be understood by the fact that the heat of formation for InN (34 kcal/mole)[29] is much lower than that of $In_2O_3$ (221 kcal/mole).[30] The instability and subsequent oxidation of InN might thus result in N-incorporated $In_2O_3$ nanoparticles in the nanocomposite samples prepared using the InN pellets.

The average nanoparticle diameters of each sample were also calculated by measuring the sizes of at least 110 nanoparticles in each TEM image; the results are summarized in Table I. The representative histograms of particle size distribution for samples *a*, *e*, and *h* are shown in Figs. 2(a)–2(c). Note that all samples were prepared at the same RF gun power of 130 W, yielding nanoparticles of similar size. Moreover, in order to avoid the influence of the

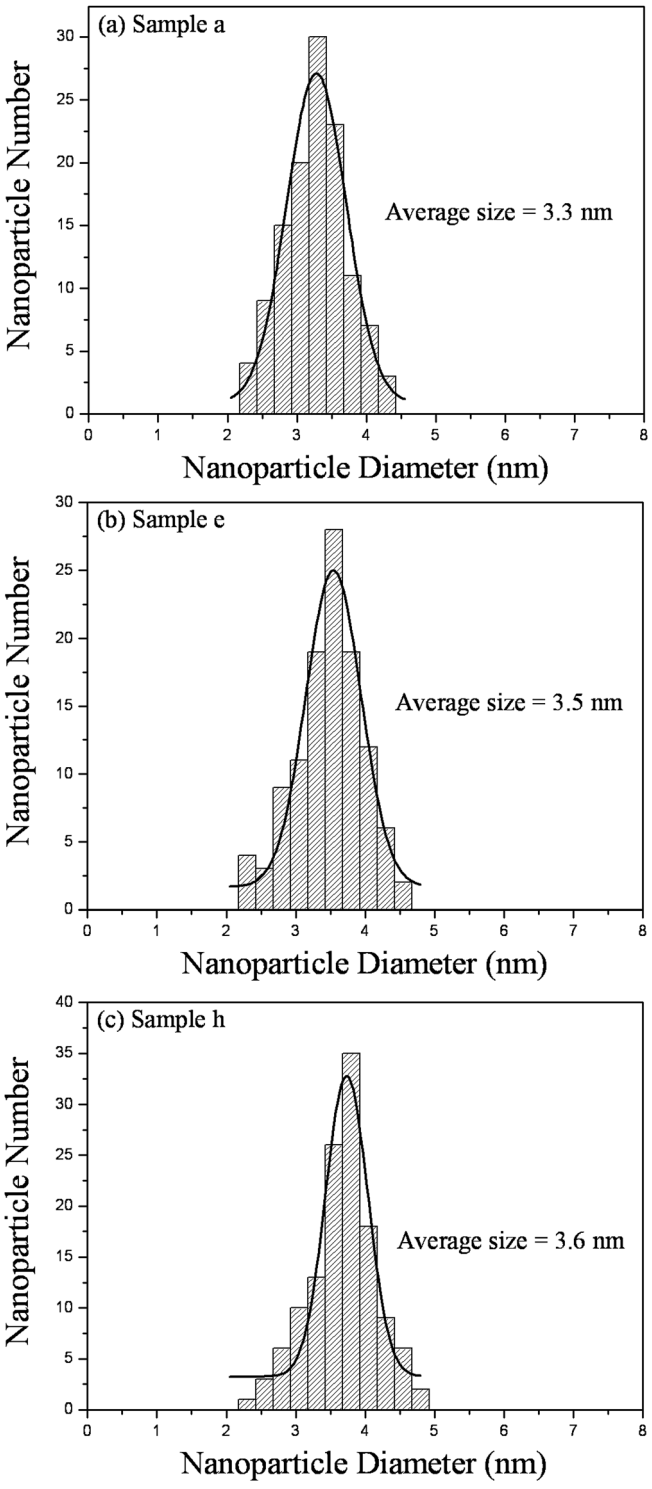


FIG. 2. The histograms of particle size distribution for samples (a) *a*, (b) *e*, and (c) *h*.

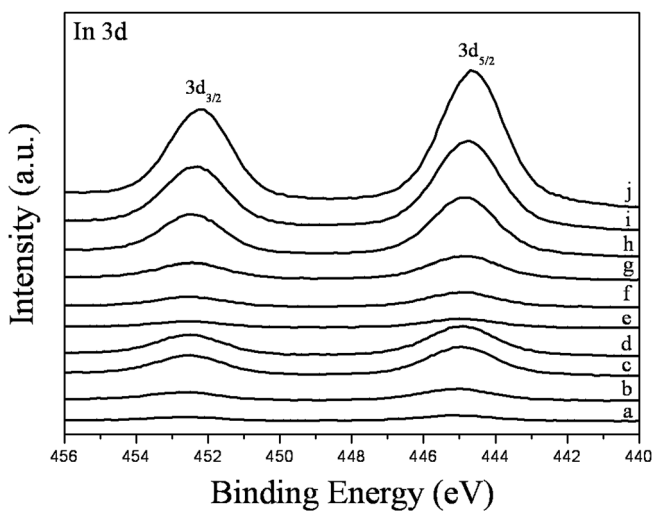


FIG. 3. In 3*d* XPS spectra for nanocomposite samples containing $In_2O_3$ nanoparticles.

quantum confinement effect, we prepared nanoparticles with sizes larger than the Bohr radius of $In_2O_3$ (i.e., 1.32 nm).[31] Calibration indicated that the diameters of the $In_2O_3$ nanoparticles were in the range of 3.2 to 3.7 nm (i.e., the radius range of 1.6 to 1.85 nm) as listed in Table I. This is suitable for discussing the N-incorporation effects in nanocomposite thin films containing $In_2O_3$ nanoparticles.

### B. XPS analysis

The N contents of nanocomposite samples were calibrated in terms of the XPS analytical results and are summarized in Table I. It can be seen that the N content of sample increases with an increasing number of InN pellets and an increasing $N_2$/Ar inlet gas flow ratio. However, the values

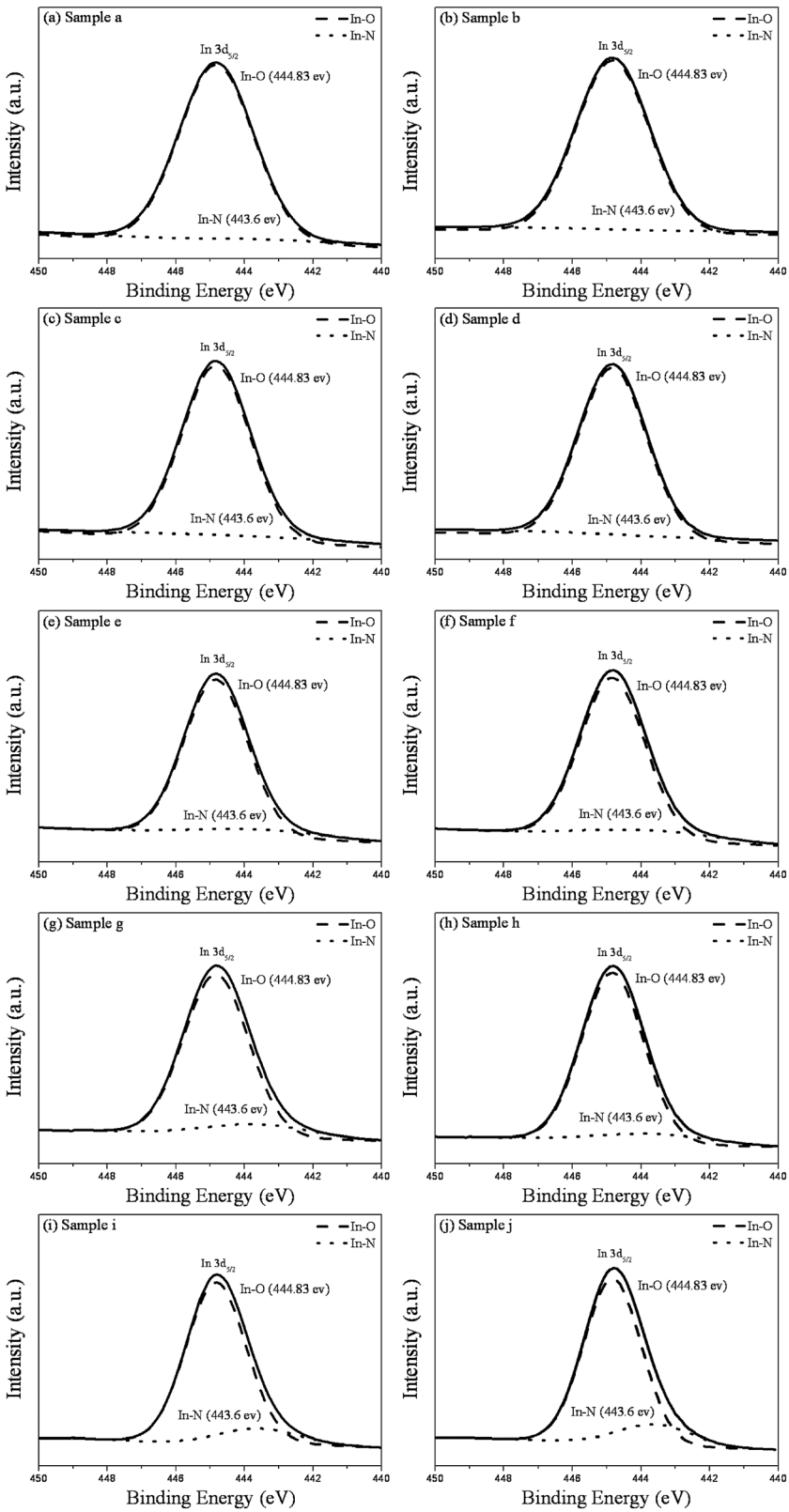


FIG. 4. In $3d_{5/2}$ XPS spectra and corresponding curve fitting results for samples *a* to *j*.

TABLE II. Summary of XPS information and curve fitting results for the nanocomposite samples containing $In_2O_3$ nanoparticles.

| | XPS integrated intensity ratio (%) | | | | | |
|---|---|---|---|---|---|---|
| | In $3d_{5/2}$ | O 1*s* | | | N 1*s* | |
| Sample | In-N bond | $O_{lattice}$ | $O^-$ | $O^{2-}$ | Si-O-N bond | In-O-N bond |
| *a* | — | 1.86 | 30.4 | 67.7 | — | — |
| *b* | — | 3.12 | 38.7 | 58.1 | — | — |
| *c* | — | 4.48 | 47.7 | 47.8 | — | — |
| *d* | — | 5.64 | 52.5 | 41.8 | — | — |
| *e* | 7.9 | 4.63 | 53.9 | 41.4 | 84.9 | 15.1 |
| *f* | 8.7 | 4.84 | 55.2 | 40.0 | 82.1 | 17.9 |
| *g* | 10.7 | 6.63 | 60.7 | 32.6 | 75.3 | 24.7 |
| *h* | 8.9 | 7.73 | 53.4 | 38.9 | 81.2 | 18.8 |
| *i* | 10.1 | 8.83 | 57.5 | 33.6 | 75.1 | 24.9 |
| *j* | 13.7 | 12.5 | 59.6 | 27.9 | 66.1 | 33.9 |

listed in Table I represent the overall N contents of the nanocomposite samples, rather than that of $In_2O_3$ nanoparticles or the $SiO_2$ matrix. Hence, the evolution of the In-N bond was further analyzed by XPS in order to discriminate the N contents in $In_2O_3$ nanoparticles.

Figure 3 depicts the In 3*d* XPS spectra for various nanocomposite samples. A slight shift of the In 3*d* XPS peaks toward the low bonding energy side can be seen for the samples prepared using InN pellets and high $N_2$/Ar gas flow ratios. With the knowledge of the In-N bonding energy (i.e., 443.6 eV),[32] deconvolution of the In $3d_{5/2}$ XPS profiles was performed using the Gaussian curve-fitting method,[33] and the results for each sample are separately presented in Figs. 4(a)–4(j). As shown by Figs. 4(a)–4(d), the In-N signals are negligibly small for samples *a-d*, which were prepared using $In_2O_3$ pellets. Hence, the incorporation of $N_2$ gas during sputtering barely facilitated the formation of In-N bonds in $In_2O_3$ nanoparticles. Subsequent XPS analysis revealed that the $N_2$-gas incorporation during sputtering in fact mainly modifies the $SiO_2$ matrix by eliminating oxygen defects and resulting in the Si-O-N bond. For samples *e-j*, the XPS peak corresponding to the In-N bond emerges, and its intensity increases with an increasing number of InN pellets. The percentages of In-N bond contents were calibrated in terms of the integrated intensity ratios of deconvoluted XPS profiles, as shown in Figs. 4(e)–4(j), and the results are listed in Table II. This illustrates that the N-incorporated $In_2O_3$ QDs can be realized by using InN pellets for sputtering deposition of nanocomposite samples.

Figures 5(a)–5(j) present the O 1*s* XPS spectra and corresponding curve-fitting results for samples *a-j*. All O 1*s* XPS spectra can be deconvoluted into three components: $O_{lattice}$ (the lattice oxygen in the $In_2O_3$ lattice; at about 530.2 eV), $O^-$ (the oxygen ions at the nanoparticle surface; at about 531.8 eV), and $O^{2-}$ (the oxygen vacancies in the $SiO_2$ matrix and $In_2O_3$ nanoparticles, or the partially weakly adsorbed oxygen species, at about 532.7 eV).[10,25] Table II summarizes the percentages of the $O^{2-}$ component and the In-O-N content for each of the nanocomposite samples, deduced by the ratios of the integrated intensities of deconvoluted XPS profiles as shown in Figs. 5(a)–5(j). Sample *a*, prepared without $N_2$-gas incorporation, contains many oxygen defects, as indicated by its high $O^{2-}$ content of 66.7%. With increasing $N_2$/Ar inlet gas flow ratio, the percentage of the $O^{2-}$ component decreases from 58.1% to 41.8% for samples *b-d*, prepared with $N_2$-gas incorporation. In conjunction with the analytical results of In 3*d* XPS spectra presented above, this implies that the $N_2$-gas incorporation may effectively eliminate oxygen defects in the $SiO_2$ matrix of nanocomposite samples. Further suppression of the $O^{2-}$ component can be seen in samples *e-j*, prepared using InN pellets. The formation of In-N bonds in nanoparticles may simultaneously improve their crystallinity.

Figure 6 presents the N 1*s* XPS spectra and corresponding curve-fitting results for samples *a-j*, calibrated in terms of the bonding energies for Si-O-N bonds (397.4–398.4 eV) and In-O-N bonds (396.4 eV).[34] According to these deconvoluted profiles, the integrated intensity ratios of Si-O-N and In-O-N bonds in samples *a-j* were calculated, and the results are listed in Table II. As shown in Fig. 6 and Table II, the In-O-N signal emerges only in samples *e-j*, prepared using InN pellets, and its intensity increases with an increasing number of InN pellets. Moreover, the peak of the N 1*s* core level was found to be located at 396.4 eV, indicating that the N atoms mainly occupy the oxygen vacancy sites rather than the interstitial sites in the $In_2O_3$ lattice.[34,35] This is in agreement with the analytical result of the O 1*s* XPS spectra, which indicates the suppression of the $O^{2-}$ component in samples *e-j*. On the other hand, the presence of a Si-O-N component in all samples indicates the formation of $SiO_xN_y$ in the $SiO_2$ matrix on account of the incorporation of $N_2$ gas during sputtering.

### C. Luminescence properties and the origins of visible-light emissions

Figure 7 shows the PL spectra of nanocomposite thin films containing $In_2O_3$ nanoparticles measured in the wavelength range of 350 to 750 nm. Since the $E_g$ of $In_2O_3$ is 3.75 eV (i.e., 330 nm), the PL emissions shown in Fig. 8 should correlate to either the carrier recombination between the conduction band (CB) edge and defect levels and/or between the defect levels and the valence band (VB) edge. Figures 8 and 9 present the curve-fitting results of the PL spectra corresponding to the samples prepared using the $In_2O_3$ and InN pellets, respectively. As shown in Fig. 8, the PL spectra of samples *a-d* are comprised of three emission bands, i.e., red, green, and blue emissions. The integrated intensity ratio of green emission decreases with increasing N content in the samples. As indicated in Table III, the integrated intensity ratio decreases from 35.3% to 30.3%. The above-presented XPS analysis indicates that $N_2$-gas incorporation mainly affects the composition of the $SiO_2$ matrix. Hence, the surface polarization effect, induced by the formation of a $SiO_xN_y$ phase in the $SiO_2$ matrix, should be considered in interpreting the PL properties of samples *a-d*. Note that the quantum confinement effect is not considered here since the radii of the $In_2O_3$ nanoparticles in all samples (1.55 to 1.9 nm) are larger than the Bohr radius of $In_2O_3$ (i.e.,

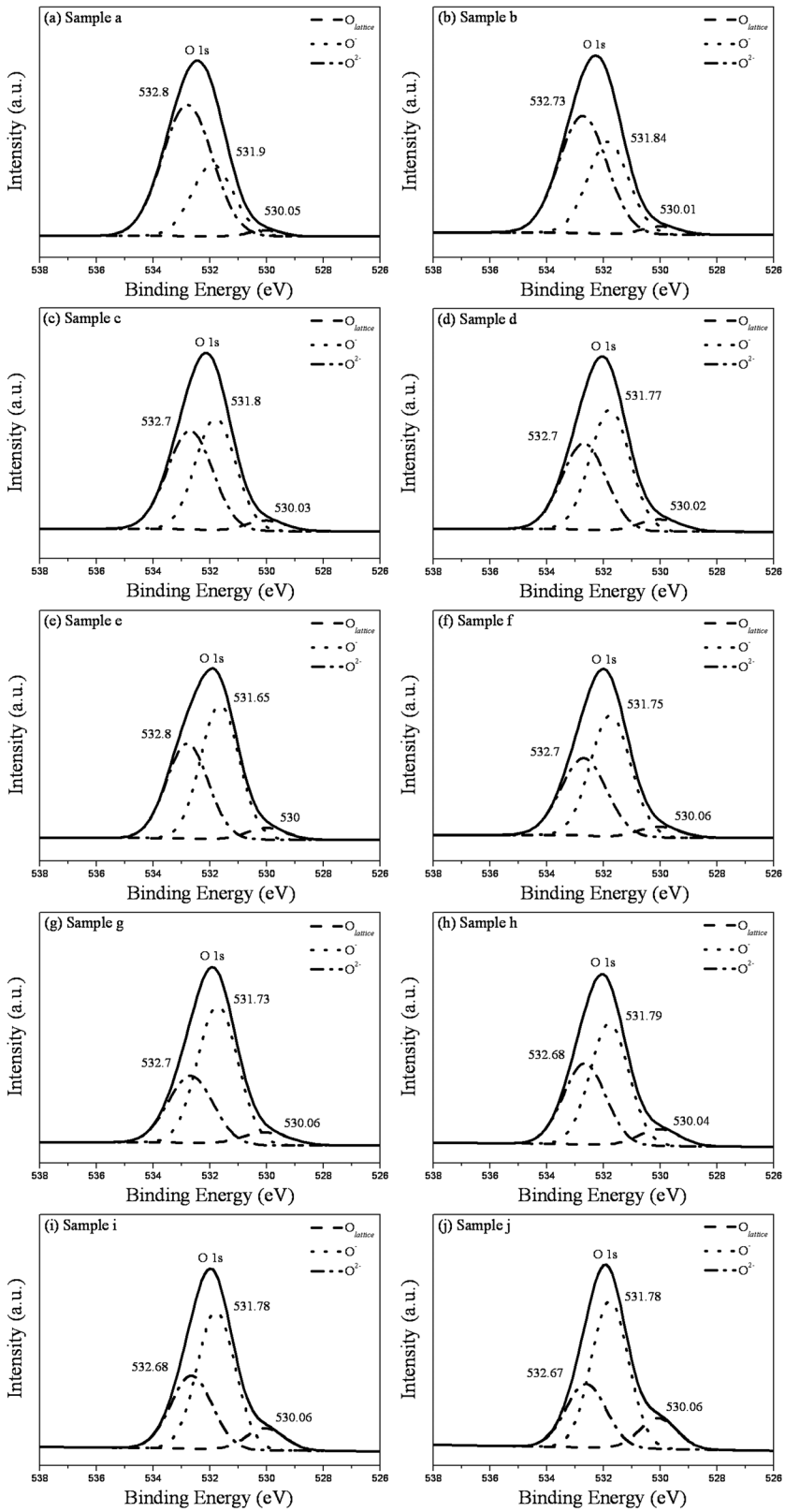


FIG. 5. O 1*s* XPS peaks and corresponding curve fitting results for samples *a* to *j*.

1.32 nm), as indicated by the particle size measurement results presented in Table I. Moreover, our previous study[31] reported that the quantum confinement effect mainly causes a blue shift of emission peaks, rather than a relative intensity change between different emissions. This is further illustrated by the PL spectra shown in Figs. 10(a) and 10(b), which depict the peak locations at 340–343 nm, i.e., the difference in $E_g$ between the samples is merely 0.03 eV. This implies that the quantum confinement effect is negligible on the PL performance of the samples prepared in this study. Figures 11(a) and 11(b) present the bonding configuration models at the interfaces of the $In_2O_3$ nanoparticle/$SiO_2$ matrix and the $In_2O_3$ nanoparticle/$SiO_xN_y$ matrix, respectively. In the $In_2O_3$-$SiO_2$ system, the $O^-$ species might react with

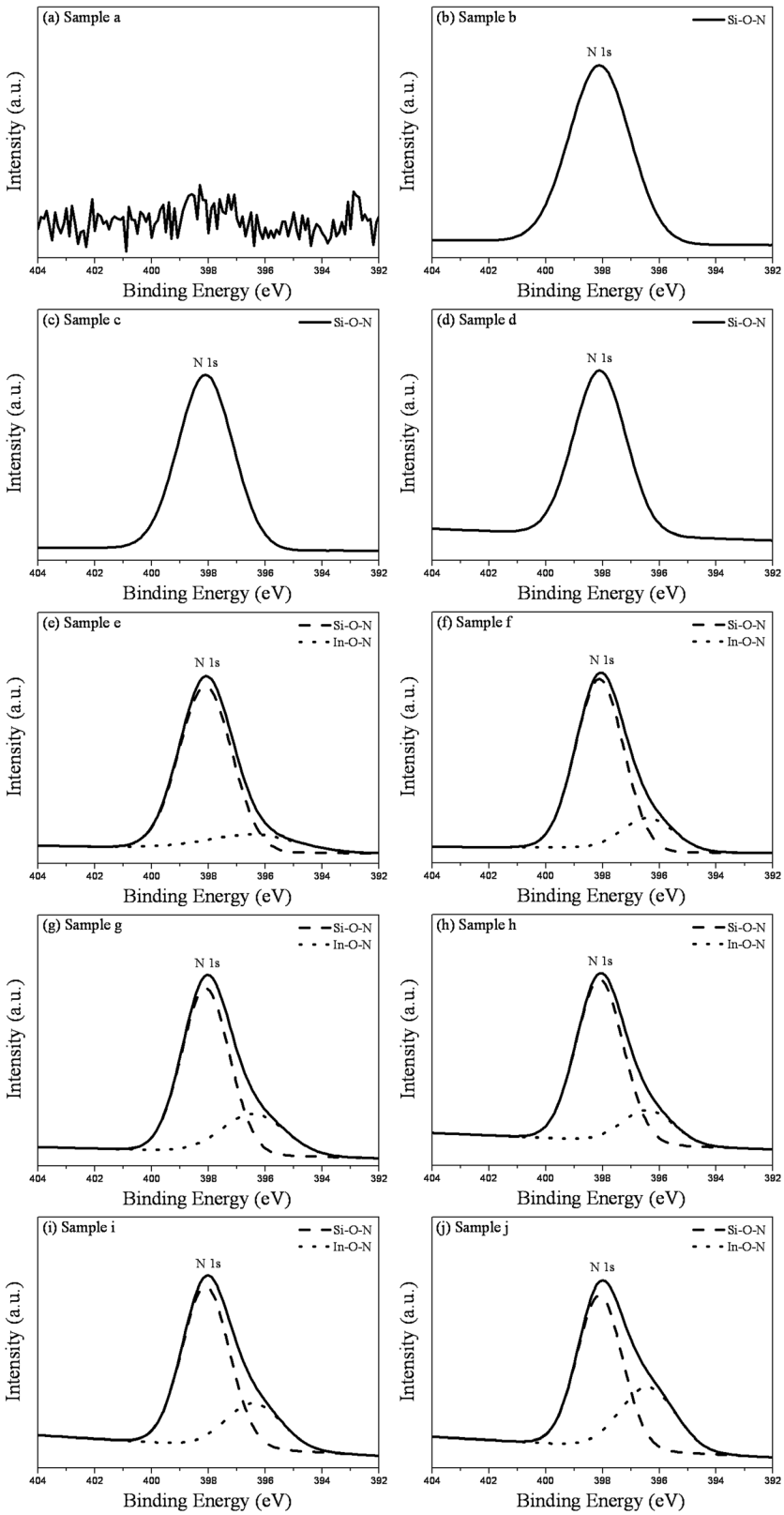


FIG. 6. N 1*s* XPS spectra and corresponding curve fitting results for samples *a* to *j*.

the ($SiO_4$) units in the $SiO_2$ matrix to form O-Si bonds on the nanoparticle surface. However, it is in the direction opposite to the Si-O bonds in the $SiO_2$ matrix, leaving a relatively weak surface polarization at the nanoparticle/matrix interface in the $In_2O_3$ QDs-$SiO_2$ system.[36] On the contrary, both the dipole moments resulting from the $O(\delta^-)$-$N(\delta^+)$ and N-Si bonds contribute to the effective polarization toward the nanoparticle surface in the $In_2O_3$-$SiO_xN_y$ system. The formation of the $SiO_xN_y$ phase in the $SiO_2$ matrix therefore enhances the surface polarization, causing the dielectric

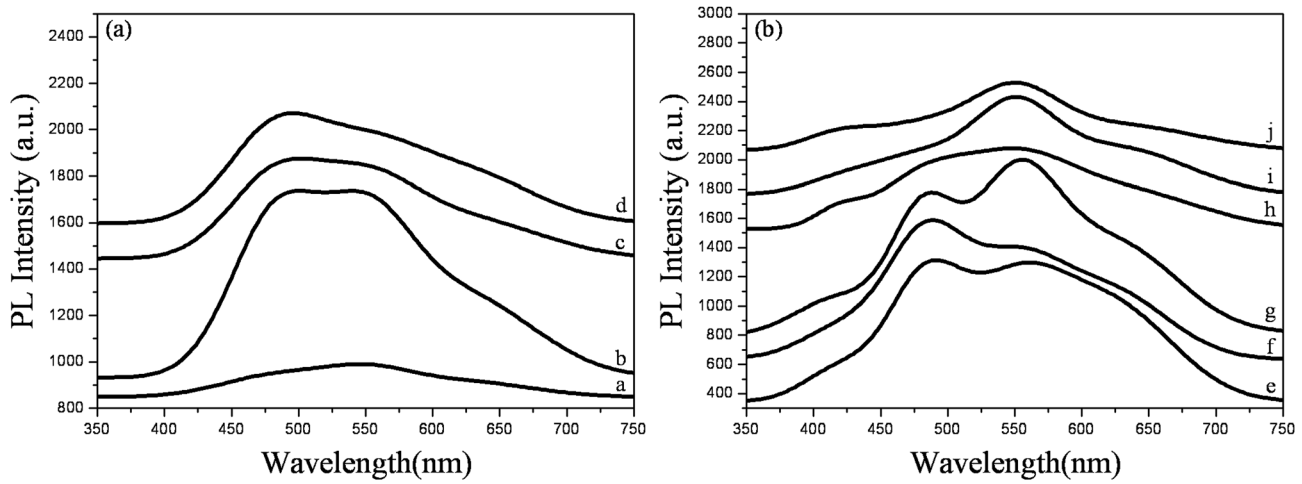


FIG. 7. PL spectra of nanocomposite samples (a) *a* to *d* prepared by using the $In_2O_3$ pellets and (b) *e* to *j* prepared by using the InN pellets.

confinement effect and consequently discouraging carrier transport in the samples.[36,37]

In the samples containing nanoscale particles, the band bending effect would generate surface and volume states due to hole migration toward the nanoparticle surface[38,39] and electron migration toward the nanoparticle interior,[40,41] respectively. A previous study found that the green emissions of $In_2O_3$ QD-$SiO_2$ nanocomposite layers are correlated to hole-related defect levels or acceptor-type defects, such as $V_{In}'''$.[10] Figure 8 and Table III depict the decrease of green emission with the increase of nitridation in the $SiO_2$ matrix of samples *a*-*d*, illustrating that the dielectric confinement effect indeed affects the physical properties relating to the surface states of nanoparticles. This also confirms that the green emission of nanocomposite thin films containing $In_2O_3$ nanoparticles originates from the acceptor defect $V_{In}'''$.

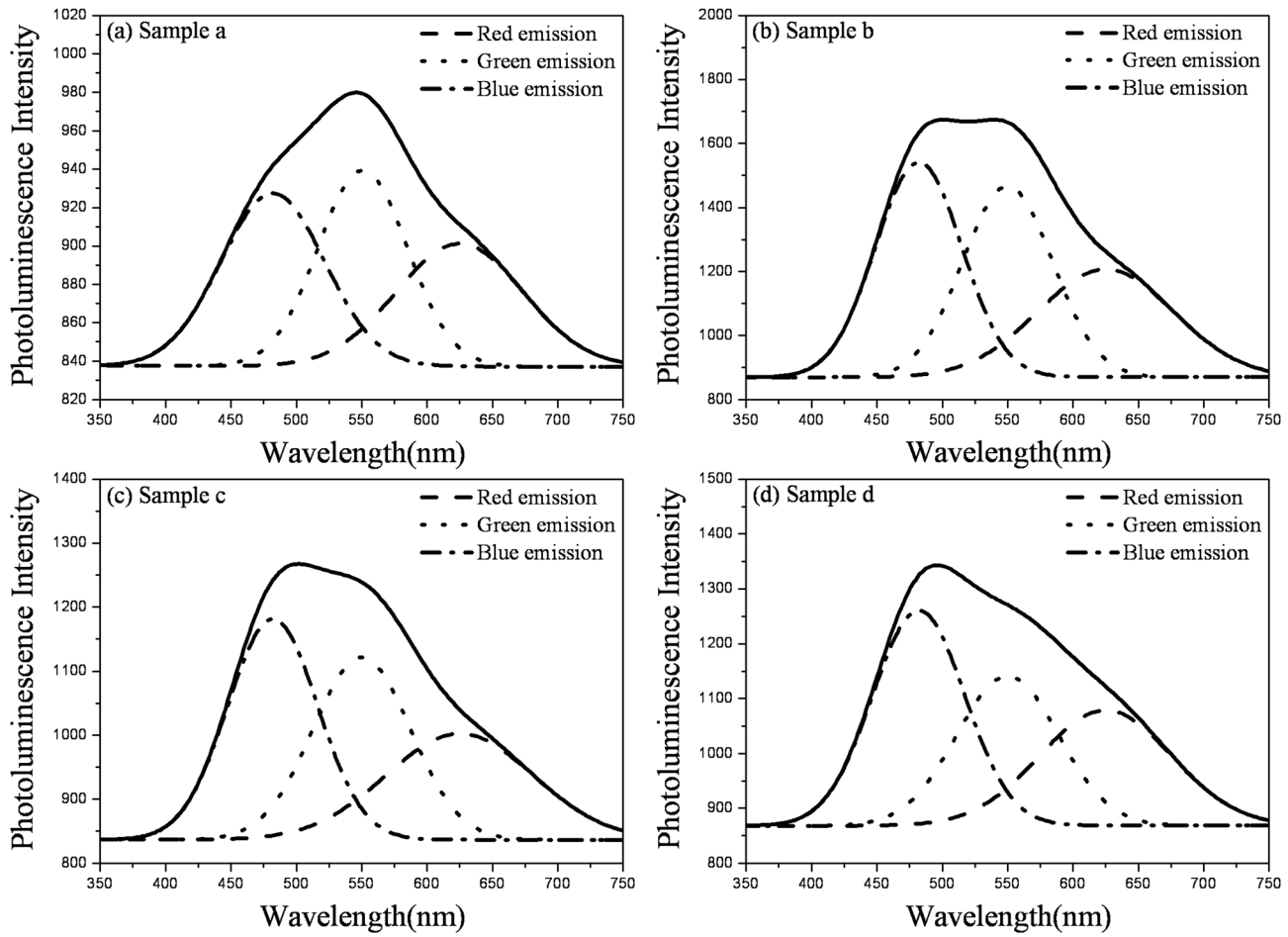


FIG. 8. Curve fitting results for PL spectra for nanocomposite samples *a* to *d* prepared by using the $In_2O_3$ pellet.

TABLE III. Summary of curve fitting results of PL spectra for the nanocomposite samples containing $In_2O_3$ nanoparticles.

| | PL peak position (nm) | | | | PL integrated intensity ratio (%) | | | |
|---|---|---|---|---|---|---|---|---|
| Sample | Red | Green | Blue | Violet | Red | Green | Blue | Violet |
| *a* | 625 | 550 | 482 | 418 | 30.6 | 35.3 | 34.2 | — |
| *b* | 625 | 550 | 482 | 418 | 29.1 | 34.0 | 36.9 | — |
| *c* | 625 | 550 | 482 | 418 | 29.4 | 33.4 | 37.2 | — |
| *d* | 625 | 550 | 482 | 418 | 30.3 | 30.3 | 39.4 | — |
| *e* | 625 | 550 | 482 | 418 | 33.8 | 34.2 | 27.5 | 4.5 |
| *f* | 625 | 550 | 482 | 418 | 33.5 | 35.4 | 26.5 | 4.7 |
| *g* | 625 | 550 | 482 | 418 | 34.9 | 36.4 | 23.4 | 5.4 |
| *h* | 625 | 550 | 482 | 418 | 35.7 | 32.7 | 26.6 | 5.1 |
| *i* | 625 | 550 | 482 | 418 | 36.9 | 33.5 | 24.0 | 5.6 |
| *j* | 625 | 550 | 482 | 418 | 38.2 | 34.5 | 21.0 | 6.4 |

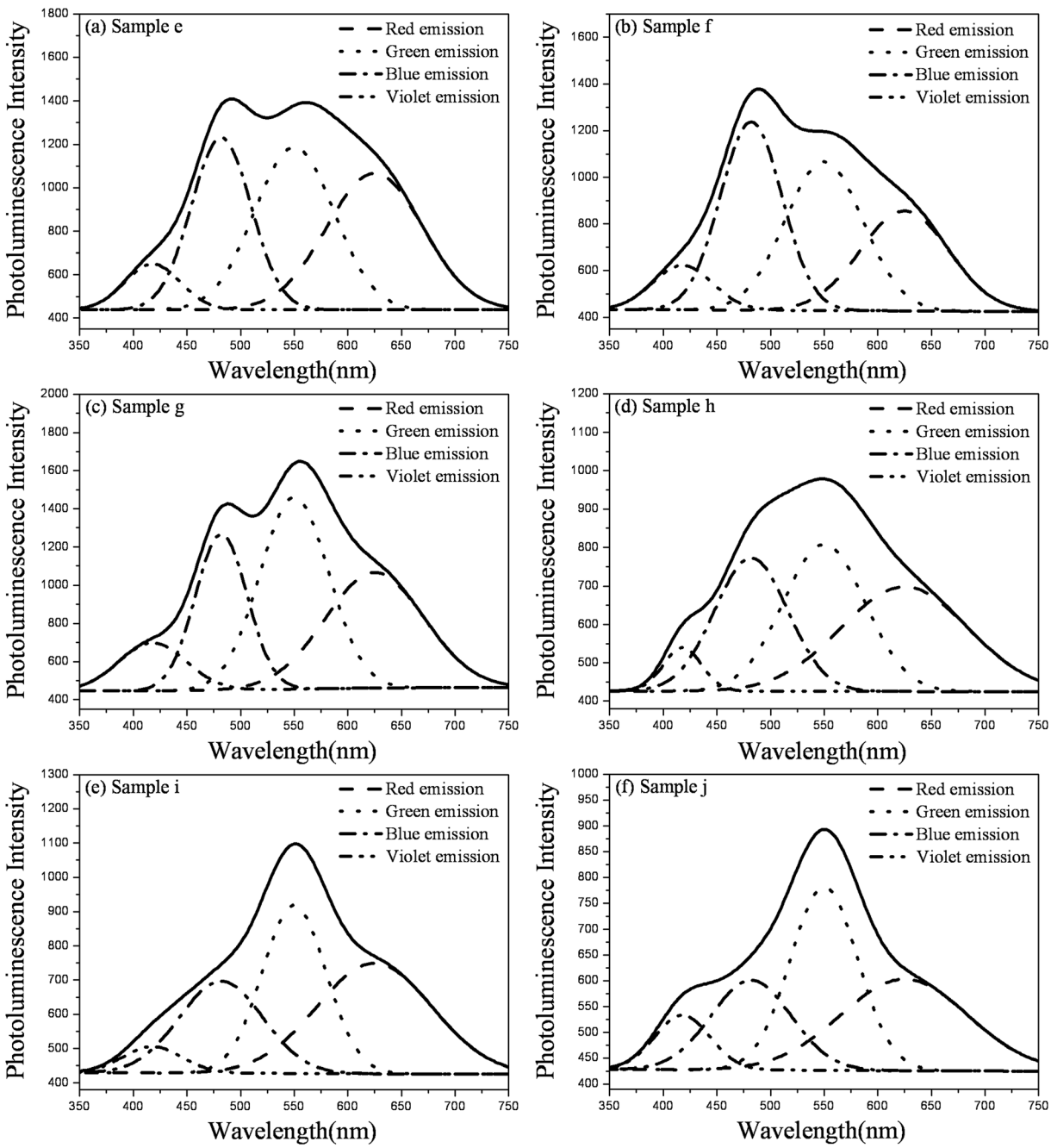


FIG. 9. Curve fitting results for PL spectra for nanocomposite samples *e* to *j* prepared by using the InN pellet.

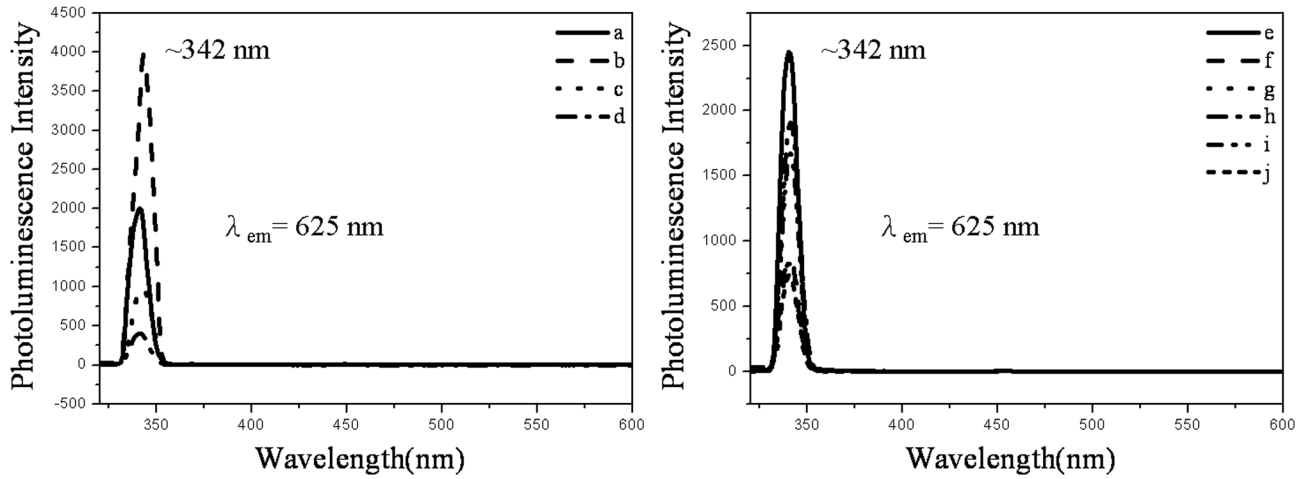


FIG. 10. PLE spectra of nanocomposite samples (a) a to d prepared by using the $In_2O_3$ pellets and (b) e to j prepared by using the InN pellets.

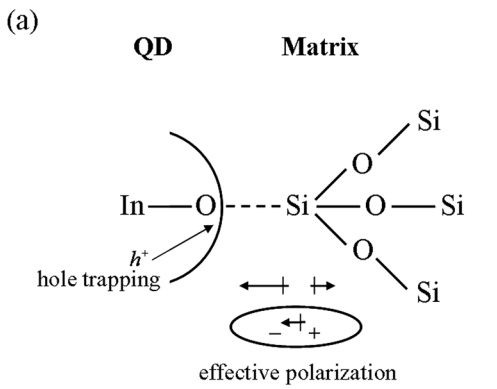


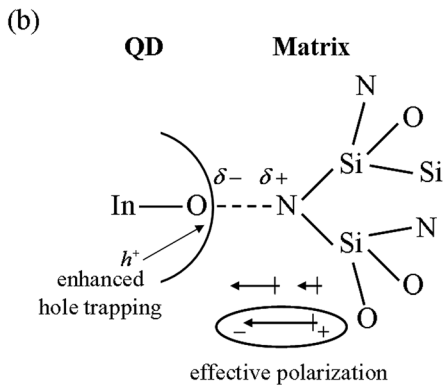


FIG. 11. Bonding configuration models at the interfaces of (a) $In_2O_3$ nanoparticle/$SiO_2$ matrix and (b) $In_2O_3$ nanoparticle/$SiO_xN_y$ matrix.

In the PL spectra of samples *e-j* prepared using InN pellets, a violet emission at 418 nm emerges in addition to the red, green, and blue emissions, as shown by their deconvolution profiles in Figs. 9(a)–9(f). The violet emission of $In_2O_3$ was also reported by Kundu and Biswas,[42] who attributed the emission to the excitonic emission of $In_2O_3$ because the shift of violet emission with the variation of excitation energy was observed. However, according to the XPS results and PL properties of samples *a-d* presented above, the violet emission should correlate with the incorporation of N elements in $In_2O_3$ nanoparticles. As listed in Table II, the integrated intensity ratios of emissions deduced from the PL spectra of samples *e-j* indicate that the intensity ratio of violet emissions increases with the increase of In-O-N bonds and vice versa for blue emission. It is inferred that an extra defect level is generated by the occupancy of N elements in oxygen sites, i.e., $N_O^-$ in N-incorporated $In_2O_3$ nanoparticles, and the transition from CB to such a defect level may be responsible for the violet emission. As for the blue emission, $N_2$-gas incorporation during sputtering may eliminate the oxygen vacancies in the oxide,[43] and previous XPS analysis indicates the suppression of the $O^{2-}$ component in samples *e-j* when the N content is increased. The decrease of blue emissions in samples *e-j* should thus correlate to the elimination of oxygen vacancies in the nanoparticles. This further confirms the assignment of the blue emission to the transition from the CB edge to oxygen defect levels of the $In_2O_3$, as reported in previous studies.[10,14,44]

## IV. CONCLUSIONS

In this study, we prepared nanocomposite thin films containing $In_2O_3$ nanoparticles using the target-attached sputtering method, utilizing InN pellets and allowing $N_2$ inlet gas flow during the deposition process. The influence of the dielectric confinement effect on the emission properties of the samples was characterized in order to clarify the debates on the emission mechanisms of $In_2O_3$. TEM analysis revealed that single-crystalline $In_2O_3$ nanoparticles were well dispersed in the $SiO_2$ matrix, and that the $In_2O_3$ is of the BCC phase type. Utilization of InN pellets for sample preparation did not imply the existence of InN nanoparticles in the samples; this was attributed to the oxidation of the InN phase as it was embedded in the $SiO_2$ matrix enriched with O elements. XPS analysis revealed that the composition of $In_2O_3$ nanoparticles is, in fact, in the form of $InO_xN_y$, and the $SiO_xN_y$ phase is observed in the $SiO_2$ matrix due to the $N_2$-gas incorporation during sputtering deposition. Nitridation in

the $SiO_2$ matrix induced the dielectric confinement effect and restrained the green emission of samples due to the enhancement of polarization on the $In_2O_3$ nanoparticle surface. Moreover, the $N_2$-gas incorporation reduced the oxygen vacancies in the $In_2O_3$ and consequently suppressed the blue emission of samples. Violet emissions were observed in the samples prepared using InN pellets, and were correlated to a new defect level, $N_O^-$, resulting from the substitution of N elements in oxygen lattice sites. The analytical results presented above confirm the mechanisms of visible-light emissions of $In_2O_3$ nanoparticles reported previously.[10]

## ACKNOWLEDGMENTS

This work was supported by National Science Council (NSC), Taiwan, R.O.C., under the Contract No. NSC100-2221-E-009-054-MY2.

[1]B. Damilano, N. Grandjean, F. Semond, J. Massies, and M. Leroux, Appl. Phys. Lett. **75**, 962 (1999).
[2]J. Lee, V. C. Sundar, J. R. Heine, M. G. Bawendi, and K. F. Jensen, Adv. Mater. **12**, 1102 (2000).
[3]N. V. Tkach and R. B. Fartsushinskiĭ, Phys. Solid State **45**, 1347 (2003).
[4]N. Daldosso, M. Luppi, S. Ossicini, E. Degoli, R. Magri, G. Dalba, P. Fornasini, R. Grisenti, F. Rocca, L. Pavesi, S. Boninelli, F. Priolo, C. Spinella, and F. Iacona, Phys. Rev. B **68**, 085327 (2003).
[5]Y. Y. Peng, T. E. Hsieh, and C. H. Hsu, J. Phys. D: Appl. Phys. **40**, 6071 (2007).
[6]M. Mazzera, M. Zha, D. Calestani, A. Zappettini, L. Lazzarini, G. Salviati, and L. Zanotti, Nanotechnology **18**, 355707 (2007).
[7]A. Murali, A. Barve, V. J. Leppert, S. H. Risbud, I. M. Kennedy, and H. W. H. Lee, Nano Lett. **1**, 287 (2001).
[8]M. Kumar, V. N. Singh, F. Singh, K. V. Lakshmi, B. R. Mehta, and J. P. Singh, Appl. Phys. Lett. **92**, 171907 (2008).
[9]S. Kar and S. Chaudhuri, Chem. Phys. Lett. **422**, 424 (2006).
[10]Y. R. Lyu and T.-E. Hsieh, "A Characterization on Emission Property of $In_2O_3$-$SiO_2$ Nanocomposite Thin Films," Surf. Coat. Technol. (in press).
[11]Z. B. Zhou, R. Q. Cui, Q. J. Pang, Y. D. Wang, F. Y. Meng, T. T. Sun, Z. M. Ding, and X. B. Yu, Appl. Surf. Sci. **172**, 245 (2001).
[12]S. Bianchi, E. Comini, M. Ferroni, G. Faglia, A. Vomiero, and G. Sberveglieri, Sens. Actuators B **118**, 204 (2006).
[13]Y. X. Liang, S. Q. Li, L. Nie, Y. G. Wang, and T. H. Wang, Appl. Phys. Lett. **88**, 193119 (2006).
[14]M. J. Zheng, L. D. Zhang, G. H. Li, X. Y. Zhang, and X. F. Wang, Appl. Phys. Lett. **79**, 839 (2001).
[15]M. S. Lee, W. C. Choi, E. K. Kim, C. K. Kim, and S. K. Min, Thin Solid Films **279**, 1 (1996).
[16]A. Orlandi, M. Rontani, G. Goldoni, F. Manghi, and E. Molinari, Phys. Rev. B **63**, 045310 (2001).
[17]A. Franceschetti and A. Zunger, Appl. Phys. Lett. **76**, 1731 (2000).
[18]L. Bányai, P. Gilliot, Y. Z. Hu, and S. W. Koch, Phys. Rev. B **45**, 14136 (1992).
[19]L. E. Brus, J. Chem. Phys. **80**, 4403 (1984).
[20]H. Yoshimura, J. N. Schulman, and H. Sakaki, Phys. Rev. Lett. **64**, 2422 (1990).
[21]G. Allan, C. Delerue, M. Lannoo, and E. Martin, Phys. Rev. B **52**, 11982 (1995).
[22]J. Linnros, N. Lalic, P. Knápek, K. Luterová, J. Kočka, A. Fejfar, and I. Pelant, Appl. Phys. Lett. **69**, 833 (1996).
[23]S. Das, S. Chakrabarti, and S. Chaudhuri, J. Phys. D: Appl. Phys. **38**, 4021 (2005).
[24]B. Alperson, G. Hodes, I. Rubinstein, D. Porath, and O. Millo, Appl. Phys. Lett. **75**, 1751 (1999).
[25]Y. Y. Peng, T. E. Hsieh, and C. H. Hsu, Nanotechnology **17**, 174 (2006).
[26]Q. Guo, O. Kato, and A. Yoshida, J. Appl. Phys. **73**, 7969 (1993).
[27]O. Ambacher, M. S. Brandt, R. Dimitrov, T. Metzger, M. Stutzmann, R. A. Fisher, A. Miehr, A. Bergmaier, and G. Dollinger, J. Vac. Sci. Technol. B **14**, 3532 (1996).
[28]J. C. Zolper, J. Cryst. Growth **178**, 157 (1997).
[29]J. B. MacChesney, P. M. Bridenbaugh, and P. B. O'Connor, Mater. Res. Bull. **5**, 783 (1970).
[30]B. R. Natarajan, A. H. Eltoukhy, J. E. Greene, and T. L. Barr, Thin Solid Films **69**, 217 (1980).
[31]Y. R. Lyu and T. E. Hsieh, ECS Solid State Lett. **1**, R9–R12 (2012).
[32]X. D. Pu, J. Chen, W. Z. Shen, H. Ogawa, and Q. X. Guo, J. Appl. Phys. **98**, 033527 (2005).
[33]J. H. Noggle, *Practical Curve Fitting and Data Analysis: Software and Self-Instruction for Scientists and Engineers* (Ellis Horwood, Hemel Hempstead, 1993).
[34]W. Yin, D. V. Esposito, S. Yang, C. Ni, J. G. Chen, G. Zhao, Z. Zhang, C. Hu, M. Cao, and B. Wei, J. Phys. Chem. C **114**, 13234 (2010).
[35]T. D. Veal, P. D. C. King, P. H. Jefferson, L. F. J. Piper, C. F. McConville, H. Lu, W. J. Schaff, P. A. Anderson, S. M. Durbin, D. Muto, H. Naoi, and Y. Nanishi, Phys. Rev. B **76**, 075313 (2007).
[36]Y. Y. Peng, T. E. Hsieh, and C. H. Hsu, J. Mater. Res. **23**, 1155 (2008).
[37]M. A. Reshchikov, H. Morkoc, S. S. Park, and K. Y. Lee, Appl. Phys. Lett. **81**, 4970 (2002).
[38]Y. J. Lee and J. L. Gary, in *IEEE Photovoltaic Specialists Conference* (1994), p. 287.
[39]H. H. Mueller and M. J. Schulz, IEEE Trans. Electron Devices **44**, 1539 (1997).
[40]M. G. Bawendi, W. L. Wilson, L. Rothberg, P. J. Caroll, T. M. Jedju, M. L. Steigerwald, and L. E. Brus, Phys. Rev. Lett. **65**, 1623 (1990).
[41]V. Esch, B. Fluegel, G. Khitrova, H. M. Gibbs, Xu Jiajin, K. Kang, S. W. Koch, L. C. Liu, S. H. Risbud, and N. Peyghambarian, Phys. Rev. B **42**, 7450 (1990).
[42]S. Kundu and P. K. Biswas, Chem. Phys. Lett. **414**, 107 (2005).
[43]N. Umezawa, K. Shiraishi, T. Ohno, H. Watanabe, T. Chikyow, K. Torii, K. Yamabe, K. Yamada, H. Kitajima, and T. Arikado, Appl. Phys. Lett. **86**, 143507 (2005).
[44]W. S. Seo, H. H. Jo, K. Lee, and J. T. Park, Adv. Mater. (Weinheim, Ger.) **15**, 795 (2003).